Remote Sens. **2015**, *7*, 8391-8415; doi:10.3390/rs70708391

OPEN ACCESS

remote sensing

ISSN 2072-4292

www.mdpi.com/journal/remotesensing

Article

Effect of the Aerosol Model Assumption on the Atmospheric Correction over Land: Case Studies with CHRIS/PROBA Hyperspectral Images over Benelux

Cecilia Tirelli [1,*], Gabriele Curci [1,2,†], Ciro Manzo [3,†], Paolo Tuccella [1,4,5,6]
and Cristiana Bassani [3,†]

[1] CETEMPS, University of L'Aquila, Via Vetoio, Coppito, 67100 L'Aquila, Italy;
E-Mails: gabriele.curci@aquila.infn.it (G.C.); paolo.tuccella@aquila.infn.it (P.T.)

[2] Department of Physical and Chemical Sciences, University of L'Aquila, Via Vetoio, Coppito, 67100 L'Aquila, Italy

[3] Institute for Atmospheric Pollution Research (IIA), Italian National Research Council (CNR), Research Area of Rome 1, Via Salaria km 29,300, Monterotondo Scalo, 00016 Rome, Italy;
E-Mails: c.manzo@iia.cnr.it (C.M.); cristiana.bassani@iia.cnr.it (C.B.)

[4] Sorbonne Universités, UPMC Univ. Paris 06, Université Versailles St-Quentin, CNRS/INSU, LATMOS-IPSL, UMR, 8190 Paris, France

[5] NUMTECH, 6 Allee Alan Turing, CS 60242, 63178 Aubiere, France

[6] Laboratoire de Météorologie Dynamique, Ecole Polytechnique, 91128 Palaiseau, France

† These authors contributed equally to this work.

* Author to whom correspondence should be addressed; E-Mail: cecilia.tirelli@infn.aquila.it;
Tel.: +39-0862-433708.

Academic Editors: Alexander A. Kokhanovsky and Prasad S. Thenkabail

Received: 12 April 2015 / Accepted: 16 June 2015 / Published: 26 June 2015

Abstract: Surface reflectance has a central role in the analysis of land surface for a broad variety of Earth System studies. An accurate atmospheric correction, obtained by an appropriate selection of aerosol model, is the first requirement for reliable surface reflectance estimation. In the aerosol model, the type is defined by the physical and chemical properties, while the loading is usually described by the optical thickness at 550 nm. The aim of this work is to evaluate the radiative impact of the aerosol model on the surface reflectance obtained from Compact High Resolution Imaging Spectrometer (CHRIS) hyperspectral data over land by using the specifically developed algorithm CHRIS Atmospherically Corrected Reflectance

Imagery (CHRIS@CRI) based on the 6SV radiative transfer model. We employed five different aerosol models: one provided by the AERONET inversion products (used as reference), three standard aerosol models in 6SV, and one obtained from the output of the GEOS-Chem global chemistry-transport model (CTM). The results obtained for the two case studies selected over Benelux show that in the absence of AERONET data on the scene, the best performing aerosol model is the one derived from CTM output.

Keywords: atmospheric correction; aerosol model; hyperspectral; CHRIS; CHRIS@CRI; GEOS-Chem; FlexAOD

---

1. Introduction

The surface reflectance estimation is a crucial parameter for the quantitative analysis of land surface properties in geological, agricultural, and urban studies, as well as for long-term applications of social benefits [1–3]. To obtain reliable estimations of surface reflectance from satellite, the images must be corrected considering the presence of water vapour, trace gases, and aerosol particles in the overlying atmosphere. Hyperspectral remote sensing provides the potential for more accurate and detailed information extraction than any other type of remotely sensed data [4,5].

The atmospheric correction algorithms for land have evolved over the years, from earlier scene-based empirical approaches [6–8] to more advanced methods based on rigorous radiative transfer modelling [9–13]. New methods also include spectral smoothing, topographic correction, and adjacency effect correction. The combined use of models and empirical procedures has been proposed in a few papers [14–16]. The magnitude of aerosol effects in remotely sensed data mainly depends on aerosol type and amount, observation geometry, and the wavelength [2]. Several studies have shown the crucial role of aerosol optical thickness at 550 nm in atmospheric transfer modelling [17–24] and on the atmospheric correction of multispectral and hyperspectral data for ocean and land properties retrieval [25–31]. The combination of satellite hyperspectral data, ground measurements, and model-based analysis allows complete information datasets for accurate surface reflectance retrieval [32].

The aim of this work is to evaluate the radiative impact of the aerosol model on the results of the atmospheric correction designed for Compact High Resolution Imaging Spectrometer (CHRIS/PROBA) hyperspectral data acquisitions over land. The reflectance is obtained using the CHRIS Atmospherically Corrected Reflectance Imagery (CHRIS@CRI) algorithm [21,25], a physically based atmospheric correction algorithm developed specifically for CHRIS data by adapting the vector version of the Second Simulation of a Satellite Signal in the Solar Spectrum (6SV) radiative transfer code [33], an improved open-source code of the 6S [27]. The aerosol radiative impact was investigated, comparing the reflectance obtained by applying the CHRIS@CRI algorithm with different aerosol models: one using AERONET (AERosol RObotic NETwork) sun-photometer retrievals, three standard types implemented in 6SV, and one extracted from the detailed simulations of the chemistry-transport model GEOS-Chem. The microphysical properties (size distribution, the real and imaginary part of the refractive index) and the optical properties (single scattering albedo and asymmetry parameter) from AERONET are considered the reference to inter-compare results obtained using other models.

This paper is organized as follows: in Section 2, an overview of the area test case of this study is presented and a complete description of the data used in the study is provided, while in Section 3, the CHRIS@CRI atmospheric correction is described. In Section 4, the results are shown for the aerosol properties analysis and for the comparison of the reflectance values obtained after the atmospheric correction process. The conclusions are finally summarized in Section 5.

2. Data

2.1. Study Area

As a test case, the area of Benelux was considered (see Figure 1). In particular, the CHRIS images were selected over the urban center of Brussels (Belgium) and the continental site of Cabauw (the Netherlands), in which two AERONET sun photometers are installed. The AERONET sun photometer in Brussels is installed on the roof (120 m high) of The Belgian Institute for Space Aeronomy, in Uccle (south of Brussels), beside the Royal Observatory of Belgium and the Royal Meteorological Institute of Belgium. The AERONET sun photometer of Cabauw is located in the western part of the Netherlands in a polder 0.7 m below average sea level. In addition, the aircraft measurements collected in May 2008 during the EUCAARI-LONGREX [34] campaign were also used to validate the simulated aerosol fields from the chemistry-transport model.

2.2. Data Description

2.2.1. AERONET Measurements

The automatic tracking sunphotometer CIMEL CE-318 measures the direct spectral solar irradiance between 340 and 1020 nm (440 nm, 670 nm, 870 nm, and 940 nm are standard wavelengths) and sky radiance for solar almucantar or principal plane scenario at six nominal bands (440, 670, 870, and 1020 nm) [35]. It provides the aerosol optical thickness at the six nominal bands, the columnar content of water vapour (wv), and ozone (O_3) from the direct component of the solar irradiance. The aerosol micro-physical and optical properties (aerosol complex refractive index, single scattering albedo, and the scattering phase function) are retrieved from the diffuse components of sky radiance on four bands (442, 668, 870, and 1020 nm) at specific angles [36]. Aerosol optical depth data and inversion products are provided for three data quality levels: Level 1.0 (unscreened), Level 1.5 (cloud-screened), and Level 2.0 (cloud-screened and quality-assured). For the atmospheric correction, Level 2.0 data were preferred when possible. However, the AERONET inversion products are often available only at quality Level 1.5, so these are usually used for atmospheric studies worldwide.

2.2.2. CHRIS Data

The CHRIS (Compact High Resolution Imaging Spectrometer) on PROBA satellite is a high resolution multi-angular imaging spectrometer, with a spectral range from 400 to 1050 nm and a spatial resolution of 17 or 34 m. CHRIS provides acquisitions up to 62 narrow and quasi-contiguous spectral bands. The specific feature of CHRIS is that it provides data from five observation angles during the same overpass. One of the main advantages of the CHRIS instrument is the high configurability of its operation mode. CHRIS is characterized by five operational modes, which are associated with the five spectral configurations (Mode 1–5). In particular, in Mode 3 (full swath, full resolution) CHRIS acquires images characterized by 17 m of nominal spatial resolution, 18 spectral bands, and 13 km of nominal swath width. The combination of the 18 spectral bands typical of this mode is specifically used for land studies. CHRIS data is supplied in HDF (Hierarchical Data Format) data files (version 4.1r3). The HDF file contains the image file and the ancillary data, such as spectral and geometric parameters. All CHRIS images in this work were acquired in Mode 3. CHRIS images were selected if simultaneous AERONET (Level 2.0 or Level 1.5) acquisition data were available. Other specific requirements for imagery acquisition were clear-sky conditions, the aerosol loading defined by an AOT (Aerosol Optical Thickness) value >0.1, and high solar irradiation (solar zenith angle < 60°). Table 1 shows date and time of selected CHRIS images and of the corresponding atmospheric aerosol data (AOT@550nm, wv, and O_3 columnar contents) from simultaneous AERONET measurements. The value of AOT@550 nm obtained from GEOS-Chem model simulations is also specified. For each case study, the solar zenith angle relative to the two CHRIS overpasses and the AERONET data quality levels are also displayed. These two parameters are important because they were used for the two images selected, as previously mentioned.

Table 1. Date and time of the two selected CHRIS images over Cabauw and Brussels (see Figure 1) and of the nearly simultaneous AERONET acquisitions. The corresponding values of the solar zenith angle (SZA), the aerosol optical thickness at 550 nm (AOT@550 nm) from AERONET data and from GEOS-Chem simulations, the water vapour (wv) and ozone (O_3) columns, and the quality level of AERONET data are also shown.

	Cabauw	**Brussels**
Date (dd/mm/yyyy)	10/05/2008	19/08/2009
Time AERONET (hh: mm)	10:27 (Level 1.5)	09:48 (Level 1.5)
Time CHRIS (hh: mm)	9:38	9:51
AOT@550 nm AERONET	0.149	0.122
AOT@550 nm GEOS-Chem	0.166	0.133
O_3 (gm^{-2})	0.373	0.314
Wv (gm^{-2})	1.058	2.598
Zenith angle (°)	37	45

3. Methods

3.1. Atmospheric Correction

An important requirement for an accurate atmospheric correction is an appropriate selection of aerosol loading and type. The aerosol optical thickness at 550 nm (AOT@550 nm) is widely used to describe the aerosol loading [26–30]. The physically based atmospheric correction algorithm CHRIS@CRI needs, as input, the aerosol AOD at 550 nm, the water vapour and ozone columnar content, and a standard or user-defined aerosol type, defined by its size distribution function (SD) and the real (m_r) and imaginary (m_i) part of the complex refractive index. The algorithm for the atmospheric correction of CHRIS images was implemented following the method reported in Bassani *et al.* [21], as shown in Figure 2.

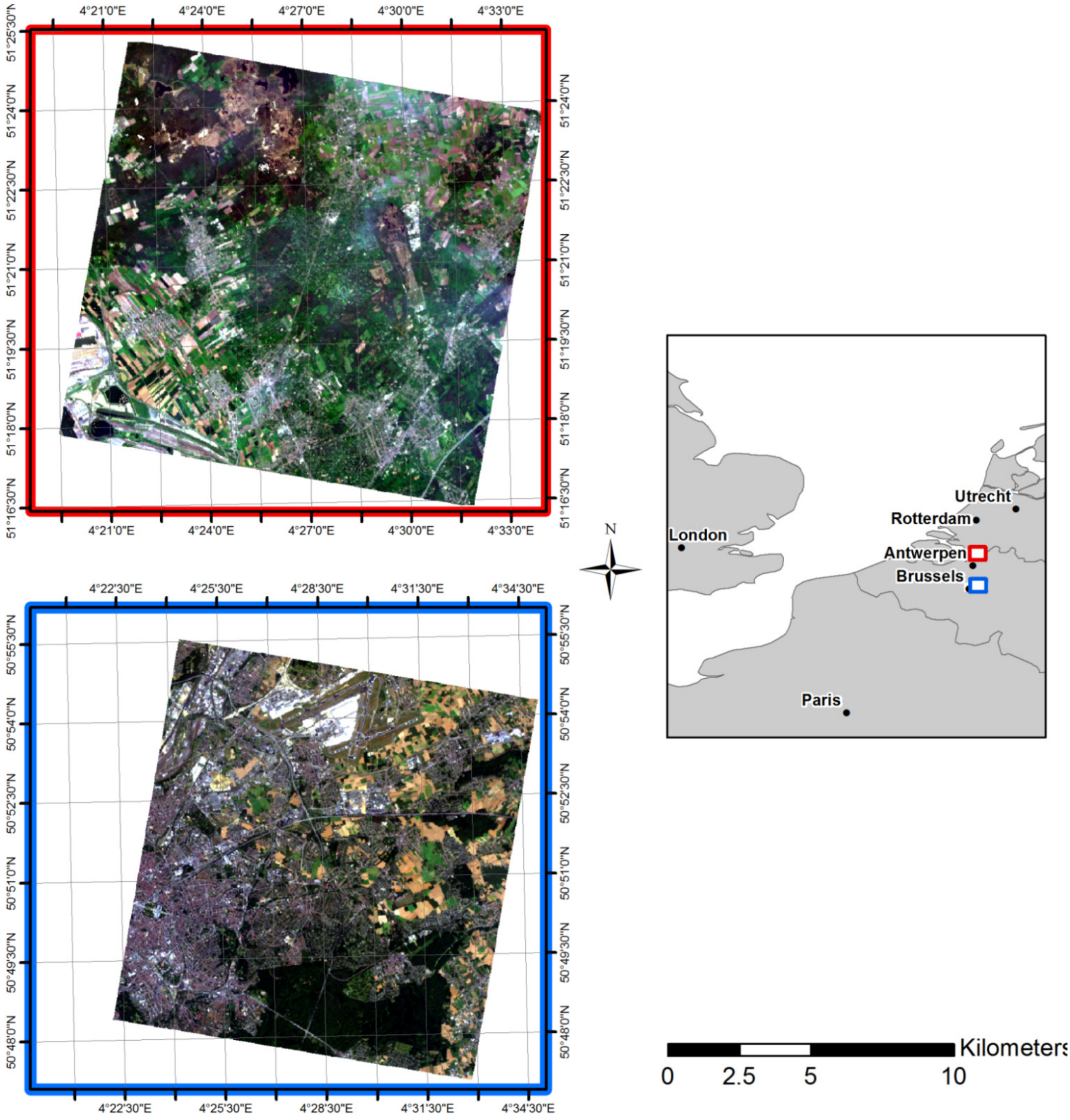

Figure 1. The two RGB (R: channel 7; G: channel 4; B: channel 1) CHRIS images selected: over Cabauw on 10 May, 2008 (red) and over Brussels on 19 August, 2009 (blue).

The at-sensor radiance definition [26] was used under the assumption of the isotropy surface to neglect the influence of the solar and viewing angles on the surface reflectance. For each CHRIS channel, the surface reflectance ρ_g [21] is computed as:

$$\rho_g = \frac{t_g \rho_{atm} - \rho_{TOA}}{S(t_g \rho_{atm} - \rho_{TOA}) - t_s t_g} \tag{1}$$

In the equation, $\rho_{TOA} = \pi L_v / \mu_s E_s$ is the top of atmosphere (TOA) reflectance, where L_v is the at-sensor radiance, E_s is the TOA solar irradiance, and μ_s is the cosine of the solar zenith angle. The other quantities in Equation (1) are the gas transmittance t_g, the atmospheric reflectance ρ_{atm} (or path radiance), the atmospheric spherical albedo S [19], and the total transmittance t_s. The latter is obtained from the downward (t^d) and upward (t^u) direction components, each one composed of the direct and diffuse component ($t^{u,d}_{dir,dif}$).

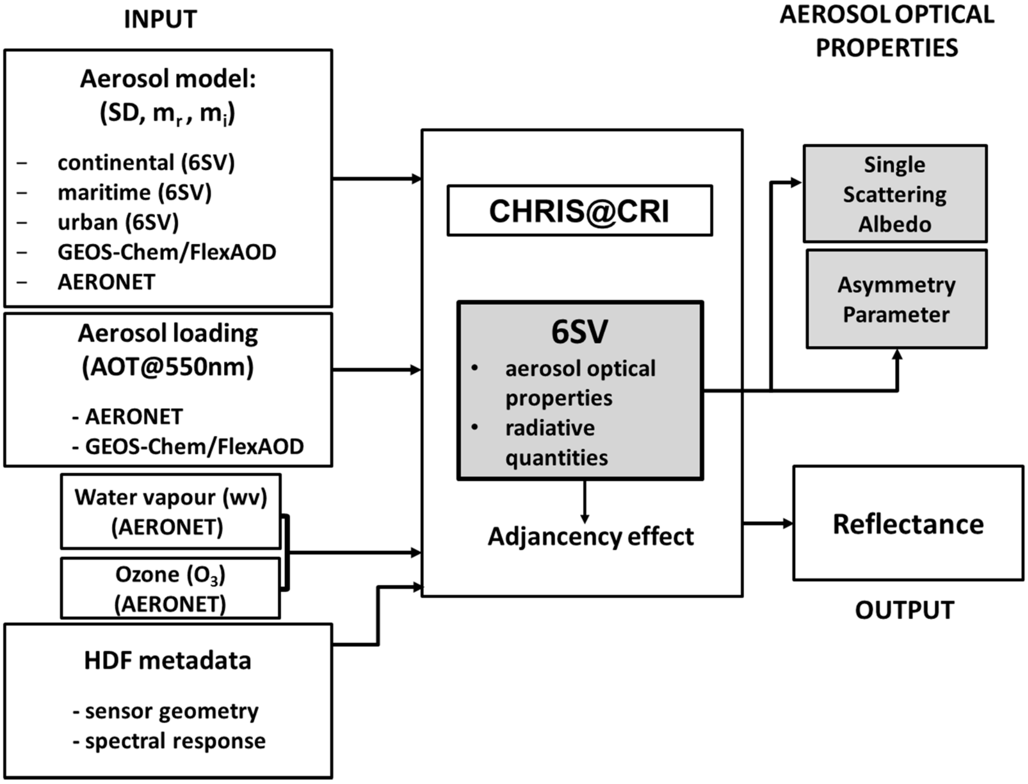

Figure 2. The diagram of the methodology developed for the atmospheric correction process of the two CHRIS images, using different aerosol models as input for the CHRIS@CRI algorithm.

The radiative quantities are simulated by a pixel-by-pixel method over a scan-line with a spectral sampling of 2.5 nm, covering the domain from 350 nm to 2.5 μm by using the latest version of 6SV. Since the pixel-by-pixel method requires a considerable computational processing time, the 6SV code runs just for the viewing geometry on a selected number of pixels, equidistant along a scan-line. The radiative quantities are then interpolated along the pixels of whole scan-line. The CHRIS@CRI algorithm computes the convolution of radiative quantities on the spectral response of CHRIS channels, assumed Gaussian with the central wavelength and the full width at half maximum (FWHM) provided by the HDF file. Furthermore, the HDF file also provides the input for the viewing geometry of the image: the longitude and latitude, observation azimuth, and zenith angles (see Figure 2). In the atmospheric correction of satellite data in the visible and near-infrared channels, it is necessary to remove the adjacency effect (see Figure 2) due to the reflection from neighbors' pixels. The surface reflectance is calculated applying the empirical formula used in atmospheric correction algorithms [21,26,27,29,30]

$$\rho(\lambda) = \rho_{g+}\frac{t^u_{dif}}{t^u_{dir}}[\rho_g - <\rho_g>] \tag{2}$$

where $<\rho_g>$ is the mean of the pixels adjacent to the viewing pixel covering the CHRIS sensors' swath (13 km^2).

As shown in the diagram of Figure 2, the runs of the CHRIS@CRI algorithm were performed with all selected aerosol models: the 6SV aerosol standard types (maritime, urban, or continental), one provided by the AERONET inversion products, and one obtained from the GEOS-Chem model simulations. The 6SV standard types (maritime, urban, and continental) are defined as a combination of the four basic aerosol components: sea-salt, water-soluble, dust-like, and soot (see Table 2). For Aerosol loading input, the values provided by AERONET and GEOS-Chem were considered.

Table 2. The volumetric mixing ratio of the four basic components (dust-like, oceanic, water-soluble, and soot) for urban, maritime, and continental 6SV standard aerosol models [19,33,37].

	Dust-Like	**Oceanic**	**Water-Soluble**	**Soot**
URBAN	0.17	0	0.61	0.22
MARITIME	0	0.95	0.05	0
CONTINENTAL	0.70	0	0.29	0.01

3.2. GEOS-Chem/FlexAOD Model

GEOS-Chem is a global chemistry-transport model (CTM) [38] for atmospheric composition driven by assimilated meteorology from the Goddard Earth Observing System (GEOS) of the NASA Global Modeling and Assimilation Office (GMAO). Here we use model version 9-01-03, which is freely available online together with full documentation at http://geos-chem.org. The meteorological data versions are GEOS-5 at a spatial resolution of 2° × 2.5° in the horizontal and 47 layers in the vertical (from the surface to 0.01 hPa), with resolution degrading from ~100 m in the first km, to ~500 m in the upper troposphere, and a few km in the mesosphere. Anthropogenic emissions of CO, NOx, SO2, NMVOCs, and primary aerosols are derived from a combination of the global EDGAR v4.2 inventory (http://edgar.jrc.ec.europa.eu/overview.php?v=42) and regional inventories as described at http://geos-chem.org. Natural and biogenic emissions from vegetation, soils, volcanoes, and lightning are also calculated.

The simulation of aerosol relies on work by [39,40] for the sulfate-nitrate-ammonium (SNA) and carbonaceous fractions. SNA simulation was recently updated with the implementation of the thermodynamic module ISORROPIA II [41] and the account for cloud water pH for in-cloud sulfate formation [42]. For carbonaceous matter, the secondary organic aerosol (SOA) module was updated with the inclusion of oxidation products from terpenes [43], isoprene [44], and aromatics [45]. Soil dust and sea salt simulation are described in [46,47], respectively.

The calculation of aerosol optical properties follows the methodology developed by [48], with updates on dust size distributions by [49]. In the version employed here, the GEOS-Chem model explicitly simulates the mass concentration of the aerosol species, and optical properties are derived from the concentration of six optical aerosol species (inorganic ions (sulfate + nitrate + ammonium), organic carbon, blank carbon, sea salts, and soil dust) assumed as spherical and externally mixed. Each species is assigned relative humidity (RH) dependent log-normal size distributions and refractive indices. Optical properties are then interpolated from the extinction efficiency, the single scattering albedo, and the polynomial expansion terms of the scattering phase function tabulated as a function of RH. The pre-calculated table is computed using the MIE code by [50].

In this work, the aerosol optical properties are calculated off-line using the post-processing tool FlexAOD [51]. The GEOS-Chem optical properties are typically calculated online and the output is given at one wavelength for the aerosol optical depth. The FlexAOD tool is used to repeat calculations at all pertinent AERONET wavelengths (440, 675, 870, 1020 nm) and all input wavelengths in the 6SV radiative transfer model (350, 400, 412, 443, 488, 515, 550, 590, 633, 670, 694, 760, 860, 1240, 1536, 1650, 1950, 2250, and 3750 nm). Moreover, the tool is used to calculate the total aerosol size distribution interpolated on the 6SV size bins and column-average values of the refractive index, the single scattering albedo, and the asymmetry parameter directly comparable to AERONET inversion products.

For each CHRIS scene presented in the manuscript, a GEOS-Chem run is carried out first in order to simulate the aerosol fields for the specific time and location of the scene. The aerosol profile extracted from the model grid point nearest to the scene is then used as input to FlexAOD to calculate the aerosol properties needed to run 6SV and compare the data with AERONET products.

4. Results

4.1. Comparison of GEOS-Chem-FlexAOD Aerosol Simulation with Aircraft Campaign Observations

The GEOS-Chem chemistry transport model is employed in this work to represent a state-of-the-art aerosol profile simulation, specific to the time and place of the satellite observation, to provide input for the atmospheric correction algorithm. The skills of GEOS-Chem in reproducing the observed aerosol profiles across the globe were summarized by [52], comparing simulations with measurements from 17 aircraft campaigns. Typically, sulfate concentrations are in the range of observed values, while organic matter is underestimated by a factor of 3–4 in polluted regions (which are of main interest here). The comparison of the campaign-average profile over the region of interest of this manuscript (Benelux) is presented in [52] for sulfate and organic matter, using data collected during the EUCAARI-LONGREX campaign [34] in the period of 6–22 May 2008. Here we present a comparison of our simulations with selected profiles collected during the EUCAARI campaign in three days (6, 8, and 12 May), close to the acquisition of the CHRIS image over Cabauw (10 May).

In Figure 3, we show the comparison of aerosol species' mass concentration, measured with the Aerosol Mass Spectrometer (AMS) [53] and the Single Particle Soot Photometer (SP2) [54], with model results. The three flights are chosen with the following criteria: (1) the flight path is an ascending or descending vertical profile, *i.e.*, long horizontal legs were not considered; and (2) the distance of the profile is within 100 km of Cabauw. This is to assure that we (1) test model skills along the vertical, which is the relevant dimension for the aerosol radiative effects we are evaluating in this study; and (2) account for the model horizontal resolution, which is approximately 200 km. Data are averaged in 200 m-thick altitude bins, and presented as mean profiles with standard deviations.

Regarding the inorganic secondary species (sulfate, ammonium, nitrate), the model under-predicts concentrations observed on 6 May, over-predicts those on 8 May, and is in the range measurement standard deviation on 12 May. On the other hand, organic matter is systematically under-predicted. The statistical summary of the comparisons presented in Table 3 confirms that the average model fractional bias (MFB) of inorganic species is less than 10%. That the root mean square error (RMSE) is substantially larger than the mean bias points out that the model bias is unsystematic rather than systematic for those species. The correlation of simulated concentrations with measurements is between 0.46 and 0.56 for those species, indicating a discrete capability of the model in reproducing the observed variability. The model underestimates organic matter on average by a factor of two (MFB of −99%), and this bias is largely systematic (RMSE is similar to MB). The deficiency in simulating organic matter is a well-recognized problem of current CTMs and it is mostly attributable to unconstrained secondary organic aerosol sources [55]. The variability of the observations is poorly represented (correlation of 0.17). The black carbon concentration is overestimated by a factor of two (MFB of +91%), and the bias is systematic (RMSE is almost equal to MB). The correlation is relatively poor at 0.15. Although a factor of two uncertainty in reproducing black carbon (BC) observations is expected [56], we speculate that the positive systematic bias may be due to a too-long BC lifetime in the model, which is due to an underestimated wet deposition term as recently reported [57].

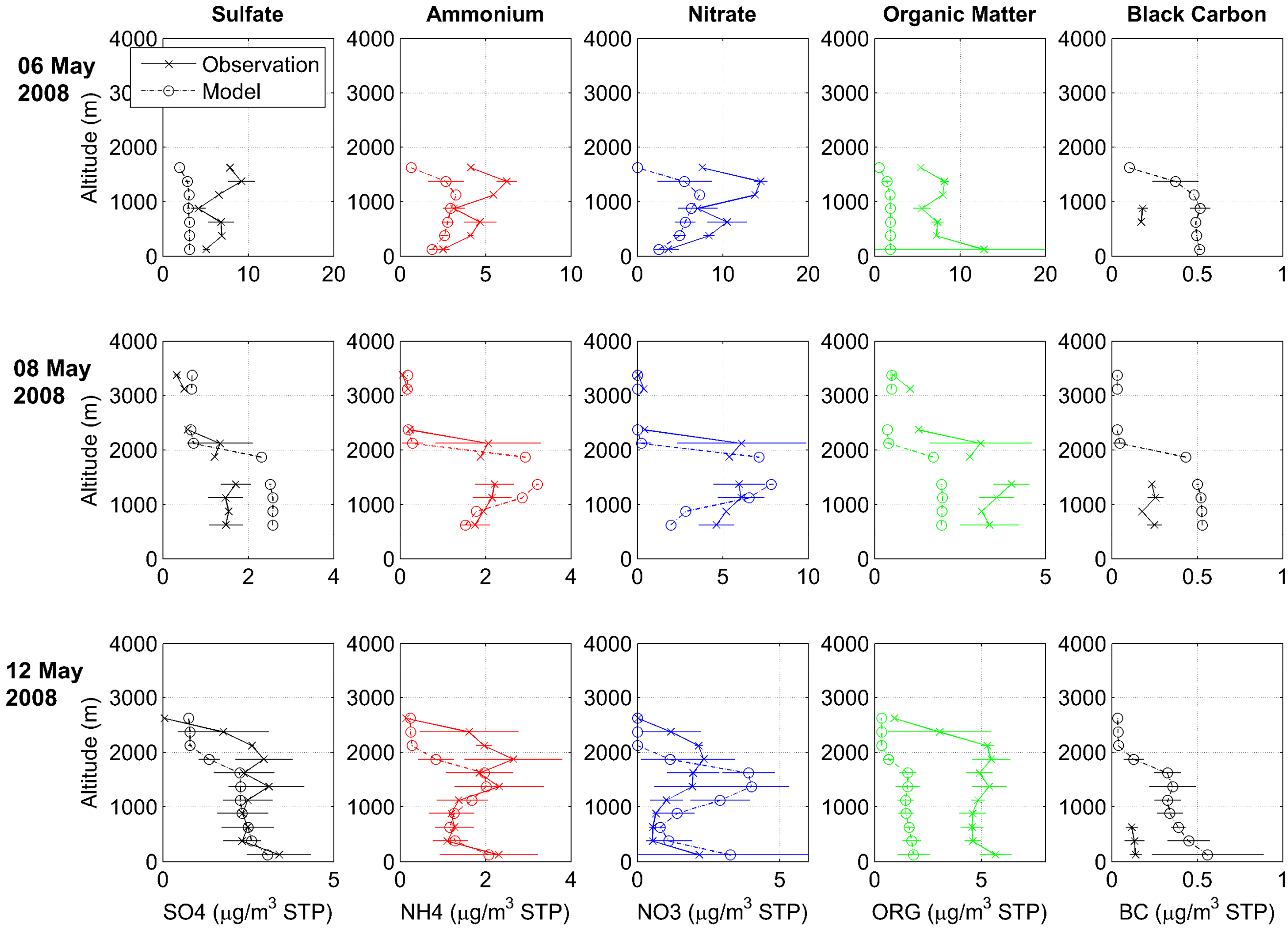

Figure 3. Comparison of observed and modelled aerosol species profiles during May, 2008 over Cabauw. From left to right, the columns show the concentration of sulfate, ammonium, nitrate, and organic matter in aerosol particles. STP refers to standard atmospheric conditions of pressure and temperature (1 atm, 273 K). From top to bottom, results are show for three flights on 6, 8, and 12 May, 2008, respectively. Data are averaged in 200 m–thick altitude bins, and the error bars denote the standard deviation.

Table 3. Statistical indices of the comparison of observed and modelled aerosol species concentration relative to flights shown in Figure 3. Statistical indices are defined in the Appendix.

	Sulfate	Ammonium	Nitrate	Organic Matter	Black Carbon
MB (μg/m^3)	−0.58	−0.22	−0.18	−3.5	+0.31
MFB (%)	−8.1	−6.6	−4.0	−99	+91
RMSE (μg/m^3)	1.7	1.1	2.9	4.8	0.33
r	0.46	0.46	0.56	0.17	0.15

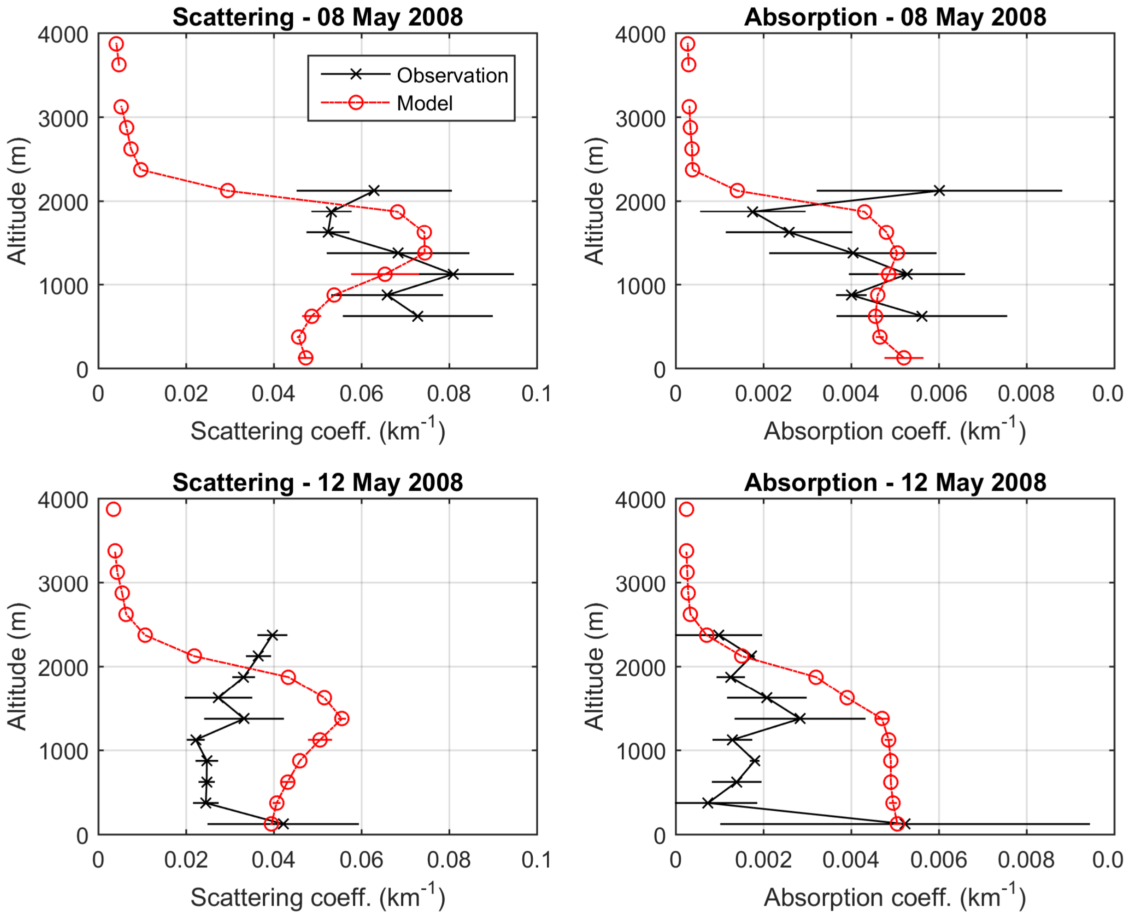

Figure 4. Comparison of observed and simulated scattering and absorption coefficient profiles during the same flights shown in Figure 2. Data of flight on 6 May were not collected. Model values were calculated capping the ambient relative humidity at 30% in order to be consistent with measurement method [34].

In Figure 4, we compare the observed profiles of the scattering and absorption coefficients during the flight shown in Figure 3 with model calculations. The scattering coefficient for dry aerosol at 550 nm was measured by a TSI 3563 integrating nephelometer, while the absorption coefficient at 567 nm was measured by a particle soot absorption photometer (PSAP) and corrected to 550 nm [34]. For consistency with observations, model optical properties are calculated capping the ambient relative humidity to 30%. These datasets are available only for profiles taken near Cabauw on 8 and 12 May. On 8 May, the model is in the range of the observed scattering coefficient, but the shape of the profile is not accurately reproduced. This is consistent with the model overestimation of inorganic aerosol mass between 1000 and 2000 m, and a general underestimation below 1000 m. The absorption coefficient is also well-reproduced by the model. The result is somewhat surprising considering the overestimation of the black carbon profile by a factor of two. We speculate that other absorbing material (e.g., primary organic carbon) substantially contributes to the observed absorption coefficient, compensating for the model error on black carbon. On 12 May, the model overestimates both the scattering and absorption coefficients. This is inconsistent with the comparison of profiles on 8 May, because the model bias in terms of aerosol mass is similar on the two flights. We could not identify, at present, a precise reason for this discrepancy. However, we note that the profile was taken about 100 km to the northwest of Cabauw over the sea, while the profile on 8 May was taken about 50 km to the southeast of Cabauw over the continent. We thus consider the profile acquired on 8 May more representative of the model skills in showing the aerosol field over the continental site of Cabauw.

4.2. Aerosol Microphysical and Optical Properties Comparison

The aerosol microphysical properties, *i.e.*, the volume size distribution, and the real and imaginary part of the refractive index, are used in the input file of the CHRIS@CRI atmospheric correction algorithm to define the atmospheric model. Figures 5 and 6 show the comparisons between aerosol microphysical properties obtained from AERONET data, the GEOS-Chem model, and from 6SV default aerosol types for 10 May 2008 over Cabauw (CW) and for 19 August, 2009 over Brussels (BR).

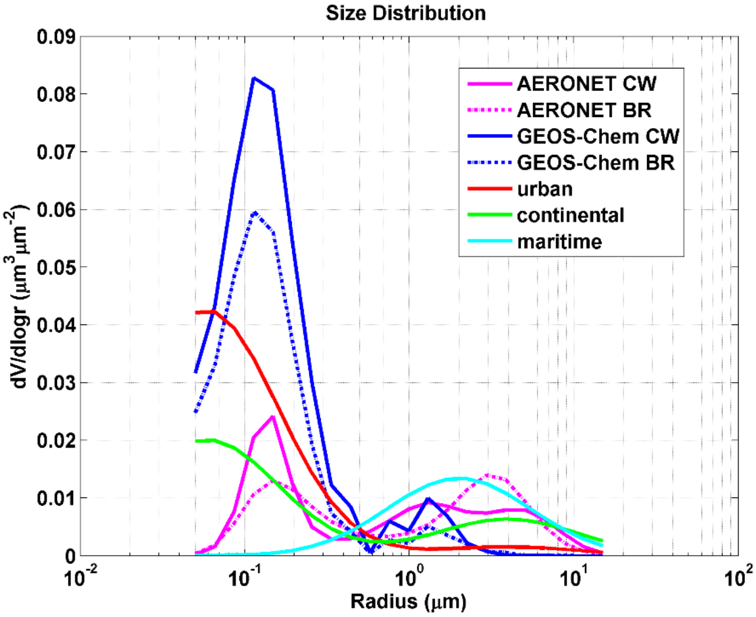

Figure 5. Aerosol volume size distributions from urban (red), continental (green), and maritime (cyan) 6SV aerosol standard types, AERONET data (magenta), and GEOS-Chem model (blue) corresponding to CHRIS images of 10 May, 2008 (solid line) over Cabauw (CW) and of 19 August, 2009 (dashed-line) over Brussels (BR).

In Figure 5, the aerosol volume size distributions are compared. The distributions from AERONET, GEOS-Chem, and 6SV continental are bimodal, while the other 6SV models are unimodal. The AERONET size distribution does not show a clear prevalence of fine or coarse particle mode. In the GEOS-Chem model, the distribution is mostly shifted to the fine mode, the peak concentration is a factor of 3–4 higher with respect to AERONET, but the diameter of the fine mode peak is consistent with inversion products. The 6SV continental model has the same magnitude of the fine mode peak concentration, but is shifted towards finer diameters with respect to AERONET. The 6SV urban fine mode is similar to that of continental, but with doubled peak concentration. The 6SV maritime model does not have a fine mode and the coarse mode is similar to that from AERONET. The GEOS-Chem and the continental coarse modes are shifted towards smaller and larger diameters, respectively. The urban has no coarse mode.

In Figure 6, the real part of the refractive index shows values near 1.5 for AERONET data. It appears spectrally constant for Brussels, while in Cabauw it increases to 1.54 for wavelengths higher than 0.7 μm. The GEOS-Chem real part of the refractive index gradually decreases from 1.52 at 400 nm to 1.48 near 1 μm. The 6SV continental values are in the same range of AERONET and GEOS-Chem, while urban and maritime are higher and lower, respectively.

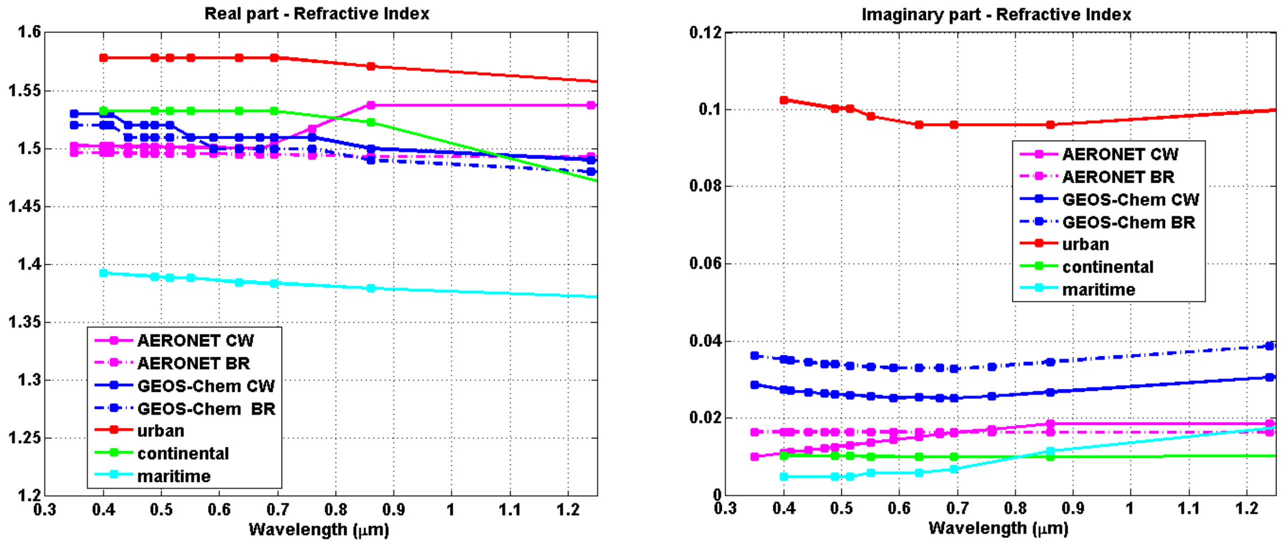

(**a**) (**b**)

Figure 6. Real (**a**) and imaginary (**b**) parts of the refractive index obtained from urban (red), continental (green), and maritime (cyan) 6SV aerosol standard types, AERONET data (magenta), and GEOS-Chem model (blue) corresponding to CHRIS images of 10 May, 2008 (solid line) over Cabauw (CW) and of 19 August, 2009 (dashed-line) over Brussels (BR).

For the imaginary part, AERONET data show in both sites spectrally constant values near 0.02. The GEOS-Chem imaginary part is higher, near 0.03, while the 6SV continental and maritime models are between 0.01 and 0.02. The urban model shows values near 0.1 over the whole spectral range, defining the absorbing behavior of this aerosol type.

In Figure 7a,b, the single scattering albedo (SSA) and asymmetry parameter (g) values are respectively shown for values obtained by AERONET inversion products and for the values simulated with MIE and AEROSOL subroutine of 6SV using microphysical properties alternatively from the five aerosol models considered in this paper. The values obtained directly from AERONET measurements, as inversion products, are completely superimposed on those obtained from 6SV calculations, as expected.

For the SSA, AERONET shows values near 0.9, while GEOS-Chem values decrease gradually from near 0.85 to 0.6–0.7. The underestimation of the SSA with respect to AERONET is expected in the

GEOS-Chem simulation, because of the overestimated concentration of the highly absorbing black carbon, as reported in the previous section. The continental aerosol has values near 0.9, nearly superimposed on those of AERONET, while urban and maritime values are higher and lower, respectively.

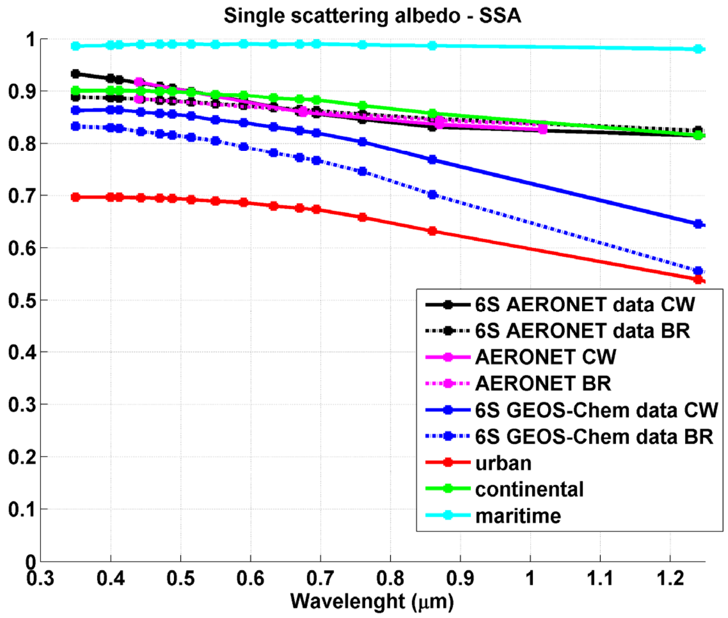

(**a**)

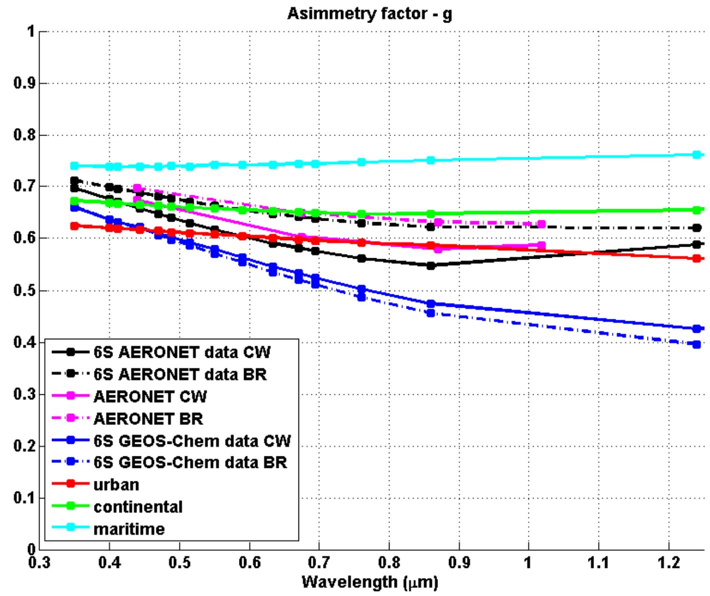

(**b**)

Figure 7. (**a**) Single scattering albedo (SSA) and (**b**) asymmetry factor (g) retrieved from AERONET and simulated with 6SV using microphysical properties from the five models.

On the 19 August, 2009 image, the asymmetry factor (g) for AERONET has values from 0.7 to 0.65, while on the 10 May, 2008 image, they decrease to 0.6. The GEOS-Chem values are lower with respect to AERONET and vary from 0.65 to 0.4, reflecting an enhanced presence of fine particles with respect to AERONET. The continental aerosol asymmetry factors are close to 0.65, nearly superimposed on those of AERONET for the Cabauw scene. Finally, the urban and the maritime aerosols have spectrally constant values of g, near 0.6 and 0.75, respectively, with the latter reflecting the prevalence of coarse particles in its size distribution.

The analysis of the microphysical aerosol properties, considering data from models (6SV and GEOS-Chem) and ground-measurements (AERONET), shows that they identify aerosol particles that are extremely different in their volume distribution function. Moreover, AERONET and GEOS-Chem show the same scattering behavior but with a higher-absorbing feature for the latter. The optical properties (g and SSA) demonstrate that the AERONET data are comparable with those of a continental aerosol as defined by the 6SV radiative transfer model, while for GEOS-Chem data analysis, the SSA and g behavior does not uniquely identify a standard aerosol, with spectral results varying from continental and urban standard types in both scenes.

The analysis of the microphysical and optical properties shows that the most sensitive parameter to determine the aerosol optical properties and consequently, the radiative behavior, is the aerosol complex refractive index. In fact, even if the volume distribution functions of AERONET and GEOS-Chem models are different, the values of SSA and g seem to be influenced mostly by the relative values of the real and imaginary part of the refractive index.

4.3. Reflectance Analysis

4.3.1. CHRIS@CRI Algorithm Validation

To validate the atmospheric correction algorithm CHRIS@CRI, the reflectance values obtained using the reference tool BEAM [58], an open-source toolbox and development platform for the viewing, analyzing, and processing of remote sensing raster data, were compared to those obtained by applying the CHRIS@CRI algorithm using AERONET data for aerosol loading and aerosol microphysical properties. To evaluate and quantify the comparison between the reflectance values, derive the percentage difference:

$$\Delta\rho_{AB} = \left(\frac{\rho_{AERONET} - \rho_{BEAM}}{\rho_{BEAM}}\right) \times 100 \tag{3}$$

This value was calculated for all spectral channels. In Figure 8, the results for the channel centered at 550 nm are shown for both scenes over Cabauw and Brussels. For the image over Cabauw, the analysis of the percentage difference at 550 nm shows a mean value of 8% with a standard deviation of 2%, while for the Brussels image, the surface reflectance map at 550 nm shows a mean value of 8.7% with a standard deviation of 4.5%. The percentage differences for the other channels are presented in Table 4. The channels 15, 16, and 17 centred at 874, 897, and 911 nm, respectively, are affected by water vapor absorption and are not considered in the analysis. We focused our attention on the effect of the aerosol model assumption on the atmospheric correction over land, considering only channels included in the atmospheric windows. The highest differences are found near the bottom of the image, over an area of very dark pixels, for which very small differences may result in large relative differences. The comparison of CHRIS@CRI results is found to be consistent with BEAM reflectances within 10% at other wavelengths, without any notable systematic bias. This lends confidence in the use of the CHRIS@CRI algorithm.

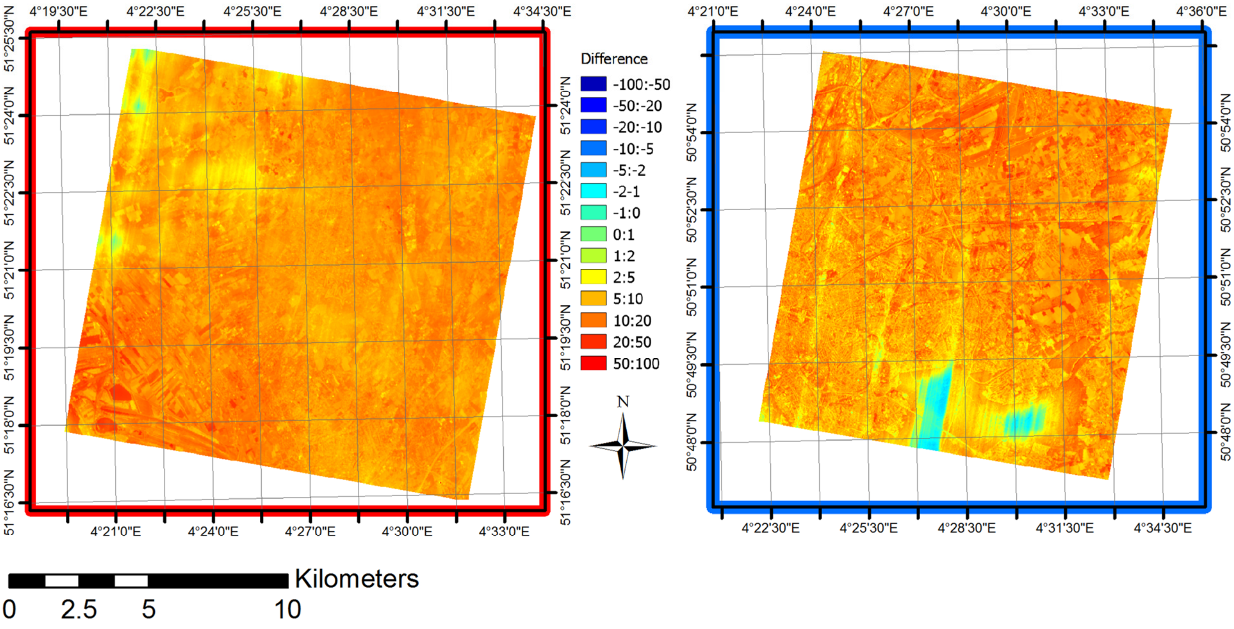

(**a**) (**b**)

Figure 8. The surface reflectance percentage difference maps at 550 nm between reflectance values obtained with CHRIS@CRI algorithm using AERONET aerosol data as input and those obtained applying BEAM atmospheric correction reference tool for (**a**) Cabauw (red) and (**b**) Brussels (blue).

Table 4. Mean and standard deviation of the relative differences of reflectance, obtained with CHRIS @CRI algorithm using input from the AERONET model compared to those obtained with the tool BEAM, for the CHRIS image over Cabauw (left) and Brussels (right).

	Cabauw		**Brussels**	
CHRIS Channel	**Mean % Difference**	**Standard Deviation**	**Mean % Difference**	**Standard Deviation**
1	−10.0	8.1	−10.4	9.6
2	4.0	4.8	10.4	8.0
3	3.2	3.0	5.2	5.4
4	8.1	2.6	8.7	4.5
5	9.5	3.3	10.2	7.2
6	8.7	3.4	10.1	6.8
7	1.4	3.2	1.0	6.7
8	2.5	3.3	3.2	7.5
9	−2.0	1.9	6.7	3.9
10	−2.0	1.4	−3.8	2.1
11	−0.1	1.3	−0.1	1.7
12	1.5	2.4	2.6	1.5
13	0.6	3.0	1.0	1.2
14	−4.0	3.2	−4.5	1.1
18	−4.9	2.7	−5.8	0.5

4.3.2. Aerosols Microphysics on Reflectance at 550 nm

The aerosol radiative impact has been quantitatively investigated, comparing the reflectance obtained by applying the CHRIS@CRI algorithm with the five different aerosol models illustrated so far. The aerosol loading is described by the aerosol optical depth at 550 nm from AERONET data for all cases except GEOS-Chem, in which the simulated value is directly used. The aerosol model defined by AERONET data is used as the reference, and the relative difference with its corresponding reflectance is used as a metric to evaluate the differences among models:

$$\Delta\rho_{(c,u,m,f)} = \left(\frac{\rho_{(c,u,m,f)} - \rho_{AERONET}}{\rho_{AERONET}}\right) \times 100 \tag{4}$$

In Figure 9, the difference at 550 nm is shown, while in Table 5, the mean and standard deviation of the differences in all pixels are reported. For both CHRIS images, the best agreement is achieved with the GEOS-Chem model (near 0% difference for Cabauw and 0.3% ± 1.2% for Brussels), and the continental model (0.40% ± 0.66% for Cabauw and 1.4% ± 1% for Brussels). The urban and maritime aerosol models overestimate and underestimate the surface reflectance value, respectively, as expected from the analysis of the microphysical properties.

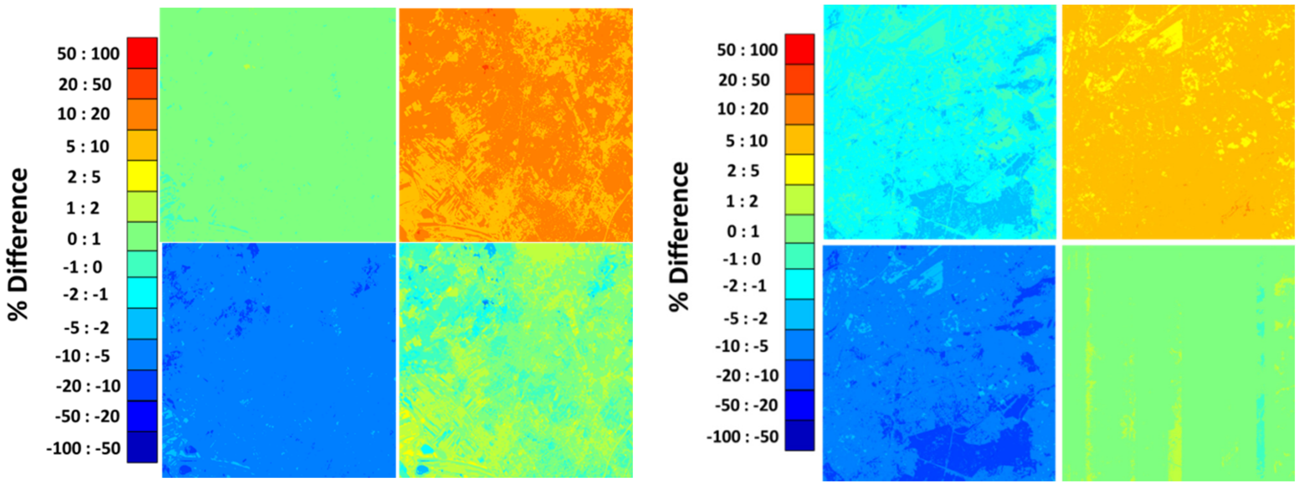

(**a**) (**b**)

Figure 9. Relative difference at 550 nm between the surface reflectance values obtained from the CHRIS@CRI atmospheric correction algorithm with the continental (top left), the urban (top right), the maritime (bottom left), and the GEOS-Chem (bottom right) models and those obtained with AERONET data, used as a reference. The results are shown for CHRIS images over (**a**) Cabauw; and (**b**) Brussels.

Table 5. Mean and standard deviation of the relative differences of reflectances obtained with different aerosol models (continental, urban, maritime, and GEOS-Chem), compared to those obtained with the AERONET model, for CHRIS images over Cabauw and Brussels.

	Cabauw		**Brussels**	
Aerosol Model	**Percentage Reflectance Difference**	**Standard Deviation**	**Percentage Reflectance Difference**	**Standard Deviation**
Continental	0.39	0.66	1.4	1.0
Urban	9.3	3.7	7.7	3.1
Maritime	−7.4	7.3	−5.00	3.4
GEOS-Chem	0.00078	0.00075	0.31	1.3

4.3.3. Reflectance Spectral Behavior

To evaluate the capability of the atmospheric correction algorithm to reproduce the reflectance spectral behavior, the surface reflectances obtained using the BEAM tool and applying to the CHRIS@CRI algorithm using AERONET data and are presented for the Cabauw and Brussels images, considering three different targets: a vegetated area, a bare soil area, and an industrial roof (Figure 10).

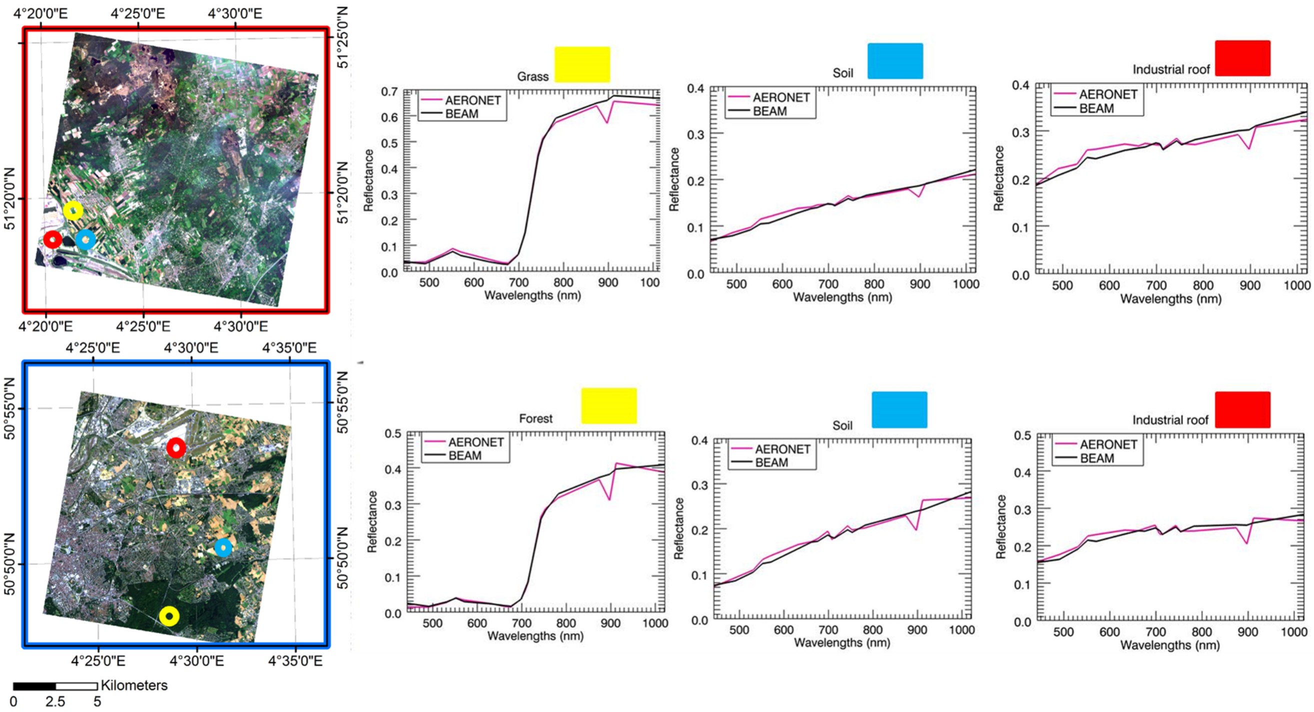

Figure 10. On the left: the two RGB (R: channel 7; G: channel 4; B: channel 1) CHRIS images over Cabauw (red) and over Brussels (blue), atmospherically corrected with the CHRIS@CRI algorithm using AERONET data. On the right: the surface reflectance obtained using the BEAM tool (black line) and applying the CHRIS@CRI algorithm using AERONET data (pink line) for three different targets (vegetated area, bare soil area and industrial roof) identified with the associated colored circles in the two images.

The two reflectance curves show the typical behavior expected for the three different targets. For the vegetated area, the reflectance values are lower than 0.1 from 400 to 700 nm, while in the NIR channels, they are higher than 0.3 for Brussels and 0.6 for the Cabauw target, respectively. The soil target displays reflectance values increasing from 0.08 (at 400 nm) to 0.2 (for Cabauw) and to 0.3 (for Brussels) (at 1000 nm), while for the brighter target, the relative values vary similarly between 0.15 and 0.3 for both scenes. A dip near 900 nm is evident in the CHRIS@CRI reflectance values. As already mentioned, the CHRIS channels centred at 874, 897, and 911 nm are affected by water vapor absorption, and this specific behavior is common to all aerosol models. The reflectance spectral behavior obtained with the two methods is in agreement with the results of the surface reflectance percentage difference $(\Delta\rho_{AB})$ analysis shown in Section 4.3.1.

In Figure 11, the surface reflectance relative differences $(\Delta\rho_{u,m,c,f})$ are presented as a function of wavelength for the two images over Cabauw and Brussels, considering the same targets.

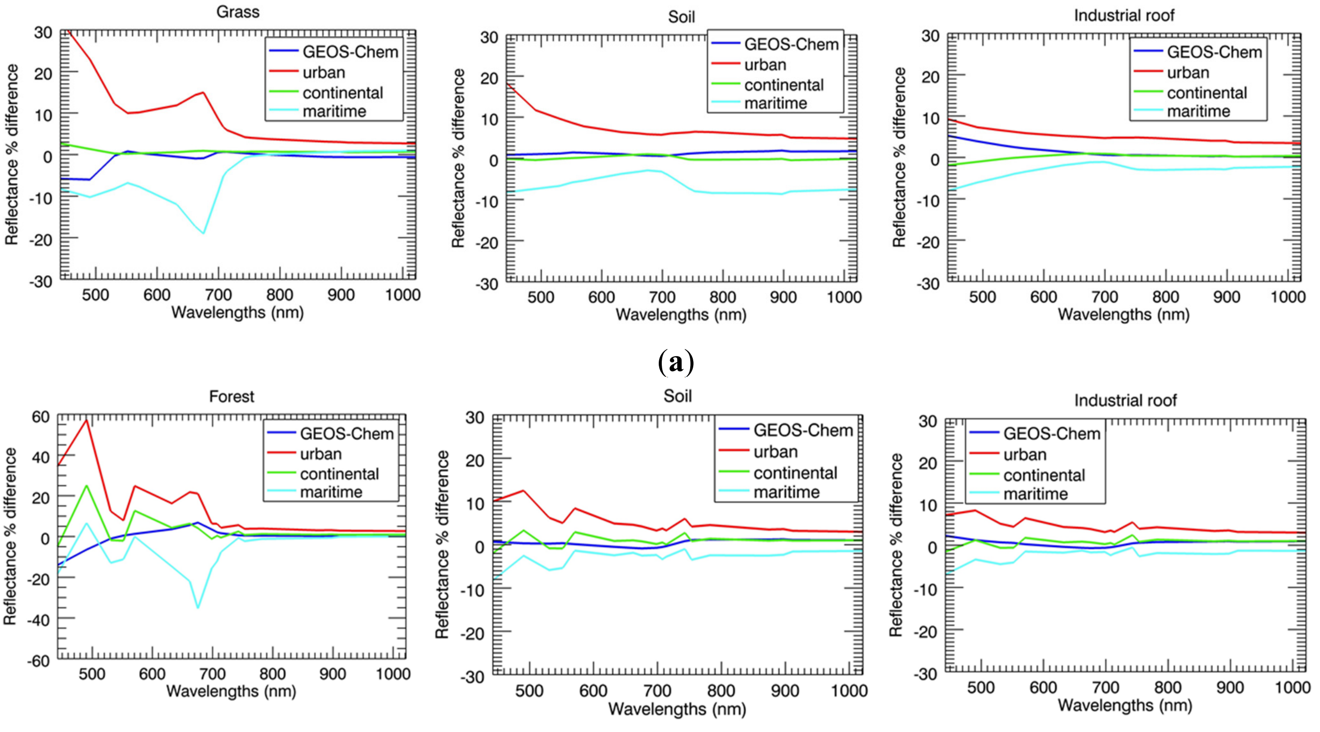

(**a**)

(**b**)

Figure 11. Spectral relative differences of the atmospherically corrected CHRIS images of (**a**) Cabauw and (**b**) Brussels calculated with the five aerosol models for vegetation (left), bare soil (center), and industrial (right) pixel types.

For both scenes, the main percentage differences are in the first part of the spectrum from 400 to 700 nm, reflecting the highest influence of aerosol scattering and absorption in the visible wavelength with respect to those in the infrared. The Cabauw analysis confirms that the use of the GEOS-Chem and the continental models for the atmospheric correction process provides similar reflectance to those obtained using sun photometer data. The other models show higher differences in the first part of the spectrum, from 400 to 700 nm, with 30% to 5% for urban and −20% to −10% for maritime models. The $(\Delta\rho_{u,m,c,f})$ values obtained for the brighter surface case (the industrial roof) are all within −10% and +10%.

For Brussels, the percentage difference values are higher, with values from −40% (for maritime aerosol at 680 nm) to 60% (for urban aerosol near 500 nm) for the dark (vegetated) target, and from −10% to 10% for the brighter ones. The GEOS-Chem aerosol model displays the best agreement with $\Delta\rho_f < 5\%$ throughout the whole spectral range, except in the first two channels for the vegetated area pixels. The continental model has values similar to GEOS-Chem, except for the forest case, where the $\Delta\rho$ has peaks around 20% in the first two channels. The urban model shows the higher $\Delta\rho$ in the whole spectral range, except from 650 to 700 nm, where the $\Delta\rho$ associated to the maritime model reaches comparatively higher values. In particular, for the urban and maritime aerosol models, the atmospheric correction leads to an overestimation and underestimation of the surface reflectance for all the CHRIS channels.

5. Conclusions

The CHRIS@CRI atmospheric correction algorithm was applied to two scenes from the CHRIS-PROBA hyperspectral satellite instrument over land (Cabauw on 10 May 2008, Brussels on 19

August 2009). The algorithm was used with five alternative aerosol models (one obtained from AERONET inversion products, three from 6SV radiative transfer model standard types, and one simulated with the chemistry-transport model GEOS-Chem) to evaluate their impact on the surface reflectance retrieval. The reflectance derived from AERONET was chosen as a reference for the inter-comparison of the results obtained from other models.

The GEOS-Chem aerosol simulation was compared with the EUCAARI-LOGREX aircraft campaign observations over Cabauw in the period of 6–12 May 2008. The average model fractional bias of inorganic species is less than 10% and the value of the root mean square error points out that the model bias is unsystematic. The model underestimates organic matter, on average, by a factor of two and this bias is proven to be largely systematic. The underestimation is consistent with current state-of-the-art chemistry-transport models. Black carbon is overestimated systematically by a factor of two, probably because of underestimated wet deposition fluxes. These results affect the microphysical characterization leading to the underestimation of the SSA simulated by 6SV reducing the accuracy of the reflectance retrieved by the CHRIS@CRI algorithm.

The general quality of the CHRIS@CRI algorithm was benchmarked against results obtained with the standard BEAM software on the two images; we found differences in the spectral surface reflectance of less than 15% and 10% for Cabauw and Brussels, respectively, which lends confidence to the use of the algorithm.

The analysis of the relative differences between the surface reflectance calculated with the different aerosol models displays a generally better agreement for the GEOS-Chem model and for the continental 6SV standard model. These results are consistent with the microphysical and optical properties of the aerosol models. The AERONET data, for both CHRIS scenes, have aerosol properties mostly similar to a continental standard type. The aerosol properties from the GEOS-Chem model are similar to AERONET, but are more absorbing and have a size distribution shifted towards the fine mode. For these test cases, the role of the real and imaginary part of the refractive index was shown to be more relevant to determining the radiative behavior rather than the size distribution function. In fact, aerosol models characterized by similar refractive index, but with very different volume size distribution, displayed a similar optical behavior.

The comparison of retrieved reflectance by CHRIS@CRI using modeled and observed microphysical properties and the reflectance obtained by aerosol standard types confirms the results shown by [59] in case of water targets. Indeed, the darkest pixels as the forest targets (Figure 10) are more sensitive to the microphysical properties adopted during the atmospheric correction.

The same analysis should be extended to other hyperspectral scenes, characterized by different atmospheric conditions and aerosol properties. In particular, it would be interesting to consider an atmospheric scene characterized by highly absorbing aerosol and characterized by a complex and documented mixing state.

This work showed that the use of output from chemistry-transport models, which is now becoming an operationally available quality product [51], may be fruitfully exploited in satellite retrieval algorithms. In fact, this study revealed that the best performing model, with respect to the observationally based atmospheric correction with AERONET input, is the detailed one, because it better reproduces the characteristics, specific in space and time, of the aerosol field on the two scenes.

Finally, this work provided a first evaluation of the impact of different microphysical properties on the radiative field characterization and, consequently, on the retrieved reflectance, showing that the most sensitive parameter is the aerosol complex refractive index.

Acknowledgments

This work was carried out as part of the PRIMES (contract n. I/017/11/0) and CLAM-PHYM (Contract No. I/015/11/0) projects, both funded by the Italian Space Agency (ASI). We are deeply thankful to Will Morgan, Gavin McMeeking, and Hugh Coe for having provided the AMS and SP2 measurements and to Ellie Highwood for having provided nephelometer and PSAP measurements, all collected during the EUCAARI/LONGREX aircraft campaign.

Author Contributions

Gabriele Curci and Cristiana Bassani designed the research. Cecilia Tirelli performed the data processing and the improvement of the atmospheric correction, and wrote the draft version of the manuscript. Gabriele Curci performed all the GEOS-Chem and FleAOD model data processing. Ciro Manzo performed image data processing and was involved in data evaluation. Cristiana Bassani developed the atmospheric correction algorithm. Paolo Tuccella was supportive in obtaining and processing the EUCAARI campaign data. All authors provided assistance in writing, editing, and organizing the manuscript.

Appendix

Definition of Statistical indices Used in Table 3

Let Obs_i and Mod_i be the observed and modeled values at time *i*, and *N* the number of observations.

- Mean Bias (MB):

$$MB = \frac{1}{N}\sum_{i=1}^{N} Mod_i - Obs_i$$

- Mean Fractional Bias (MFB):

$$MFB = \frac{1}{N}\sum_{i=1}^{N}\left(\frac{Mod_i - Obs_i}{Obs_i + Mod_i / 2}\right)\times 100$$

- Root Mean Square Error (RMSE):

$$RMSE = \sqrt{\frac{1}{N}\sum_{i=1}^{N}(Mod_i - Obs_i)^2}$$

- The Pearson's Correlation (*r*):

$$r = \frac{1}{N}\sum_{i=1}^{N} Z_i(Mod)\cdot Z_i(Obs)$$

$$Z(X) = \frac{X - \langle X \rangle}{\sigma_X}$$

where *X* is a generic vector, *Z(X)* is its standard score, and σ_X is the standard deviation.

Conflicts of Interest

The authors declare no conflicts of interest.

References

1. Bach, H.; Verhoef, W.; Schneider, K. Coupling remote sensing observation models and a growth model for improved retrieval of (geo)-biophysical information from optical remote sensing data. *Proc. SPIE* **2001**, doi:10.1117/12.413920.
2. Paronis, D.; Sykioti, O.; Kyparissis A. Effects of aerosols on narrowband indices and band depths from CHRIS/PROBA: Case study on a Phlomis fruticosa ecosystem. In Proceedings of the ESA Hyperspectral Worskhop 2010, Frascati, Italy, 17–19 May 2010.
3. Vermote, E.; Justice, C.; Csiszar, I. Early evaluation of the VIIRS calibration, cloud mask and surface reflectance Earth data records. *Remote Sens. Environ.* **2014**, *148*, 134–145.
4. Gao, B.C.; Montes, M.J.; Davis, C.O.; Goetz, A.F.H. Atmospheric correction algorithms for hyperspectral remote sensing data of land and ocean. *Remote Sens. Environ*. **2009**, *113*, S17–S24.
5. Gao, B.C.; Davis, C.O.; Goetz, A.F.H. A review of atmospheric correction techniques for hyperspectral remote sensing of land surfaces and ocean colour. In Proceedings of the IEEE International Conference on Geoscience and Remote Sensing Symposium, IGARSS 2006, Denver, CO, USA, 31 July–4 August 2006; pp. 1979–1981.
6. Kruse, F.A.; Raines, G.L.; Watson, K. Analytical techniques for extracting geologic information from multichannel airborne spectroradiometer and airborne imaging spectrometer data. In Proceedings of the International Symposium on Remote Sensing of Environment, Fourth Thematic Conference, Remote Sensing for Exploration Geology, San Francisco, CA, USA, 1–4 April 1985.
7. Roberts, D.A.; Yamaguchi, Y.; Lyon, R. Comparison of various techniques for calibration of AIS data. In Proceedings of the 2nd Airborne Imaging Spectrometer Data Analysis Workshop JPL Publication, Pasadena, CA, USA, 6–8 May 1986; pp. 21–30.
8. Conel, J.E.; Green, R.O.; Vane, G.; Bruegge, C.J.; Alley, R.E. AIS-2 radiometry and a comparison of methods for the recovery of ground reflectance. In Proceedings of the 3rd Airborne Imaging Spectrometer Data Analysis Workshop JPL Publication, Pasadena, CA, USA, 2–4 June 1987; pp. 18–47.
9. Gao, B.C.; Heidebrecht, K.B.; Goetz, A.F.H. Derivation of scaled surface reflectances from AVIRIS data. *Remote Sens. Environ.* **1993**, *44*, 165–178.
10. Richter, R. Atmospheric correction of DAIS hyperspectral image data. *Comput. Geosci.* **1996**, *22*, 785–793.
11. Adler–Golden, S.M.; Matthew, M.W.; Bernstein, L.S.; Levine, R.Y.; Berk, A.; Richtsmeier, S.C.; Acharya, P.K.; Anderson, G.P.; Felde, J.W.; Gardner, J.A.; *et al.* Atmospheric correction for short-wave spectral imagery based on MODTRAN4. In *Summaries of the Eighth JPL Airborne Earth Science Workshop JPL Publication*; Green, R.O., Ed.; Jet Propulsion Laboratory: Pasadena, CA, USA, 1999; Volume 99–17, pp. 21–29.

12. Kotchenova, S.; Vermote, E.; Matarrese, R.; Klemm, F., Jr. Validation of a vector version of the 6S radiative transfer code for atmospheric correction of satellite data. Part I: Path radiance. *Appl. Opt.* **2006**, *45*, 6762–6774.
13. Vermote, E.F.; el Saleous, N.Z.; Justice, C.O.; Kaufman, Y.J.; Privette, J.L.; Remer, L.; Roger, J.C.; Tanre, D. Atmospheric correction of visible to middle-infrared EOS-MODIS data over land surfaces: Background, operational algorithm and validation. *J. Geophys. Res.: Atmos.* **1997**, *102*, 17131–17141.
14. Clark, R.N.; Swayze, G.A.; Heidebrecht, K.; Green, R.O.; Goetz, A.F.H. Calibration to surface reflectance of terrestrial imaging spectrometry data: Comparison of methods. In Proceedings of the Summaries of the Fifth Annual JPL Airborne Earth Science Workshop, Pasadena, CA, USA, 23–26 January 1995; pp. 41–42.
15. Ben-Dor, E.; Kindel, B.; Goetz, A.F.H. Quality assessment of several methods to recover surface reflectance I using synthetic imaging spectroscopy (IS) data. *Remote Sens. Environ*. **2004**, *90*, 389–404.
16. Tuominen, J.; Lipping, T. Atmospheric correction of hyperspectral data using combined empirical and model based method. In Proceedings of the 31st EARSeL Symposium 2011, Prague, Czech Republic, 30 May–2 June 2011.
17. Kaufman, Y.J.; Wald, A.; Remer, L.A.; Gao, B.C.; Li, R.R.; Flynn, L. The MODIS 2.1 µm channel—Correlation with visible reflectance for use in remote sensing of aerosol. *IEEE Trans. Geosci. Remote Sens.* **1997**, *35*, 1286–1298.
18. Kokhanovsky, A.A.; Breon, F.-M.; Cacciari, A.; Carboni, E.; Diner, D.; di Nicolantonio, W.; Grainger, R.G.; Grey, W.M.F.; Höller, R.; Lee, K-H.; *et al.* Aerosol remote sensing over land: A comparison of satellite retrievals using different algorithms and instruments. *Atmos. Res*. **2007**, *85*, 372–394.
19. Kokhanovsky, A.A. *Aerosol Optics: Light Absorption and Scattering by Particles in the Atmosphere*; Praxis Publishing Ltd.: Chichester, UK, 2008.
20. Kokhanovsky, A.A.; Deuzé, J.L.; Diner, D.J.; Dubovik, O.; Ducos, F.; Emde, C.; Garay, M.J.; Grainger, R.G.; Heckel, A.; Herman, M.; *et al.* The inter-comparison of major satellite aerosol retrieval algorithms using simulated intensity and polarization characteristics of reflected light. *Atmos. Meas. Tech*. **2010**, *3*, 909–932.
21. Bassani, C.; Cavalli, R.M.; Pignatti, S. Aerosol optical retrieval and surface reflectance from airborne remote sensing data over land. *Sensors* **2010**, *10*, 6421–6438.
22. Shi, Y.; Zhang, J.; Reid, J.S.; Hyer, E.J.; Hsu, N.C. Critical evaluation of the MODIS deep blue aerosol optical depth product for data assimilation over North Africa. *Atmos. Meas. Tech.* **2013**, *6*, 949–969.
23. Hyer, E.J.; Reid, J.S.; Zhang, J. An over-land aerosol optical depth data set for data assimilation by filtering, correction, and aggregation of MODIS Collection 5 optical depth retrievals. *Atmos. Meas. Tech.* **2011**, *4*, 379–408.
24. Zhang, J.; Reid, J.S. MODIS aerosol product analysis for data assimilation: Assessment of over-ocean level 2 aerosol optical thickness retrievals. *J. Geophys. Res.: Atmos* **2006**, *111*, 10.1029/2005JD006898.
25. Bassani, C.; Cavalli, R.M.; Antonelli, P. Influence of aerosol and surface reflectance variability on hyperspectral observed radiance. *Atmos. Meas. Tech.* **2012**, *5*, 1193–1203.
26. Kotchenova, S.Y.; Vermote, E.F.; Levy, R.; Lyapustin, A. Radiative transfer codes for atmospheric correction and aerosol retrieval: Intercomparison study. *Appl. Opt.* **2008**, *47*, 2215–2226.

27. Vermote, E.F.; Tanré, D.; Deuzé, J.L.; Herman, M.; Morcrette, J.J. Second simulation of the satellite signal in the solar spectrum, 6S: An overview. *IEEE Trans. Geosci. Remote Sens.* **1997**, *35*, 675–686.
28. Kaufmann, Y.J.; Gobron, N.; Pinty, B.; Widlowski, J.L.; Verstraete, M.M. Relationship between surface reflectance in the visible and mid-IR used in MODIS aerosol algorithm—Theory. *Geophys. Res. Lett.* **2002**, *29*, doi:10.1029/2001GL01449.
29. Guanter, L.; Estellès, V.; Moreno, J. Spectral calibration and atmospheric correction of ultra-fine spectral and spatial resolution remote sensing data. Application to CASI-1500 data. *Remote Sens. Environ.* **2007**, *109*, 54–65.
30. Guanter, L.; Richter, R.; Kauffmann, H. On the application of the MODTRAN4 atmospheric radiative transfer code to optical remote sensing. *Int. J. Remote Sens.* **2009**, *30*, 1407–1424.
31. Goetz, A.F.H.; Vane, G.; Salomon, J.E.; Rock, B.N. Imaging spectroscopy for earth remote sensing, *Science* **1985**, *228*, 1147–1153.
32. Duca, R.; del Frate, F. Hyperspectral and multi-angle CHRIS-PROBA images for the generation of land cover maps. *IEEE Trans. Geosci. Remote Sens.* **2008**, *46*, 2857–2866.
33. Vermote, E.F.; Tanre, D.; Deuze, J.L.; Herman M.; Morcrette J.J. Second Simulation of the Satellite Signal in the Solar Spectrum—Vector (6SV). Available online: http://6s.ltdri.org (accessed on 12 April 2015).
34. Highwood, E.J.; Northway, M.J.; McMeeking, G.R.; Morgan, W.T.; Liu, D.; Osborne, S.; Bower, K.; Coe, H.; Ryder, C.; Williams, P. Aerosol scattering and absorption during the EUCAARI-LONGREX flights of the Facility for Airborne Atmospheric Measurements (FAAM) BAe-146: Can measurements and models agree? *Atmos. Chem. Phys.* **2012**, *12*, 7251–7267.
35. Holben, B.N.; Eck, T.F.; Slutsker, I.; Tanré, D.; Buis, J.P.; Setzer, A.; Vermote, E.; Reagan, J.A.; Kaufman, Y.; Nakajima, T.; *et al.* AERONET—A federated instrument network and data archive for aerosol characterization. *Remote Sens. Environ*. **1998**, *66*, 1–16.
36. Dubovik, O.; King, M.D. A flexible inversion algorithm for retrieval of aerosol optical properties from Sun and sky radiance measurements. *J. Geophys. Res*. **2000**, *105*, doi:10.1029/2000JD900282.
37. D'Almeida, G.A.; Koepke, P.; Shettle, E.P. *Atmospheric Aerosols: Global Climatology and Radiative Characteristics*; A.DEEPAK Publishing: Hampton, VA, USA, 1991.
38. Bey, I.; Jacob, D.J.; Yantosca, R.M.; Logan, J.A.; Field, B.; Fiore, A.M.; Li, Q.; Liu, H.; Mickley, L.J.; Schultz, M. Global modeling of tropospheric chemistry with assimilated meteorology: Model description and evaluation. *J. Geophys. Res*. **2001**, *106*, doi:10.1029/2001JD000807.
39. Park, R.J.; Jacob, D.J.; Chin, M.; Martin, R.V. Sources of carbonaceous aerosols over the United States and implications for natural visibility. *J. Geophys. Res.* **2003**, *108*, doi:10.1029/2002JD003190.
40. Park, R.J.; Jacob, D.J.; Field, B.D.; Yantosca, R.M.; Chin, M. Natural and transboundary pollution influences on sulfate-nitrate-ammonium aerosols in the United States: Implications for policy. *J. Geophys. Res*. **2004**, *109*, D15204.
41. Pye, H.O.T.; Liao, H.; Wu, S.; Mickley, L.J.; Jacob, D.J.; Henze, D.K.; Seinfeld, J.H. Effect of changes in climate and emissions on future sulfate-nitrate-ammonium aerosol levels in the United States. *J. Geophys. Res*. **2009**, *114*, doi:10.1029/2008JD010701.
42. Alexander, B.; Allman, D.J.; Amos, H.M.; Fairlie, T.D.; Dachs, J.; Hegg, D.A.; Sletten, R.S. Isotopic constraints on sulfate aerosol formation pathways in the marine boundary layer of the subtropical northeast Atlantic Ocean. *J. Geophys. Res*. **2012**, *117*, D06304.

43. Liao, H.; Henze, D.K.; Seinfeld, J.H.; Wu, S.L.; Mickley, L.J. Biogenic secondary organic aerosol over the United States: Comparison of climatological simulations with observations. *J. Geophys. Res.* **2007**, *112*, doi:10.1029/2006JD007813.
44. Henze, D.K.; Seinfeld, J.H. Global secondary organic aerosol from isoprene oxidation. *Geophys. Res. Lett.* **2006**, *33*, doi:10.1029/2006GL025976.
45. Henze, D.K.; Seinfeld, J.H.; Ng, N.L.; Kroll, J.H.; Fu, T.-M.; Jacob, D.J.; Heald, C.L. Global modeling of secondary organic aerosol formation from aromatic hydrocarbons: High- *vs.* low-yield pathways. *Atmos. Chem. Phys.* **2008**, *8*, 2405–2420.
46. Fairlie, T.D.; Jacob, D.J.; Park, R.J. The impact of transpacific transport of mineral dust in the United States. *Atmos. Environ.* **2007**, doi:10.1016/j.atmosenv.2006.09.048.
47. Jaeglé, L.; Quinn, P.K.; Bates, T.; Alexander, B.; Lin, J.-T. Global distribution of sea salt aerosols: New constraints from *in situ* and remote sensing observations. *Atmos. Chem. Phys.* **2011**, *11*, doi:10.5194/acp-11-3137-2011.
48. Martin, R.V.; Jacob, D.J.; Yantosca, R.M.; Chin, M.; Ginoux, P. Global and regional decreases in tropospheric oxidants from photochemical effects of aerosols. *J. Geophys. Res.* **2003**, *108*, doi:10.1029/2002JD002622.
49. Ridley, D.A.; Heald, C.L.; Ford, B.J. North African dust export and deposition: A satellite and model perspective. *J. Geophys. Res.* **2012**, *117*, D02202.
50. Mishchenko, M.I.; Dlugach, J.M.; Yanovitskij, E.G.; Zakharova, N.T. Bidirectional reflectance of flat, optically thick particulate laters: An efficient radiative transfer solution and applications to snow and soil surfaces. *J. Quant. Spectrosc. Radiat. Trans.* **1999**, *63*, 409–432.
51. Curci, G.; Hogrefe, C.; Bianconi, R.; Im, U.; Balzarini, A.; Baro, R.; Brunner, D.; Forkel, R.; Giordano, L.; Hirtl, M.; *et al.* Uncertainties of simulated aerosol optical properties induced by assumptions on aerosol physical and chemical properties: An AQMEII-2 perspective. *Atmos. Environ.* **2014**, doi:10.1016/j.atmosenv.2014.09.009.
52. Heald, C.L.; Coe, H.; Jimenez, J.L.; Weber, R.J.; Bahreini, R.; Middlebrook, A.M.; Russell, L.M.; Jolleys, M.; Fu, T.-M.; Allan, J.D.; *et al.* Exploring the vertical profile of atmospheric organic aerosol: Comparing 17 aircraft field campaigns with a global model. *Atmos. Chem. Phys.* **2011**, *11*, 12673–12696.
53. Morgan, W.T.; Allan, J.D.; Bower, K.N.; Highwood, E.J.; Liu, D.; McMeeking, G.R.; Northway, M.J.; Williams, P.I.; Krejci, R.; Coe, H. Airborne measurements of the spatial distribution of aerosol chemical composition across Europe and evolution of the organic fraction. *Atmos. Chem. Phys.* **2010**, *10*, 4065–4083.
54. McMeeking, G.R.; Hamburger, T.; Liu, D.; Flynn, M.; Morgan, W.T.; Northway, M.; Highwood, E.J.; Krejci, R.; Allan, J.D.; Minikin, A.; *et al.* Black carbon measurements in the boundary layer over western and northern Europe. *Atmos. Chem. Phys.* **2010**, *10*, 9393–9414.
55. Tsigaridis, K.; Daskalakis, N.; Kanakidou, M.; Adams, P.J.; Artaxo, P.; Bahadur, R.; Balkanski, Y.; Bauer, S.E.; Bellouin, N.; Benedetti, A.; *et al.* The AeroCom evaluation and intercomparison of organic aerosol in global models. *Atmos. Chem. Phys.* **2014**, *14*, 10845–10895.

56. Wang, Q.; Jacob, D.J.; Fisher, J.A.; Mao, J.; Leibensperger, E.M.; Carouge, C.C.; le Sager, P.; Kondo, Y.; Jimenez, J.L.; Cubison, M.J.; *et al.* Sources of carbonaceous aerosols and deposited black carbon in the Arctic in winter-spring: Implications for radiative forcing. *Atmos. Chem. Phys.* **2011**, *11*, 12453–12473.
57. Wang, X.; Heald, C.L.; Ridley, D.A.; Schwarz, J.P.; Spackman, J.R.; Perring, A.E.; Coe, H.; Liu, D.; Clarke, A.D. Exploiting simultaneous observational constraints on mass and absorption to estimate the global direct radiative forcing of black carbon and brown carbon. *Atmos. Chem. Phys.* **2014**, *14*, 10989–11010.
58. BEAM Home. Available online: http://www.brockmann-consult.de/cms/web/beam (accessed on 31 March 2015).
59. Bassani, C.; Manzo, C.; Braga, F.; Bresciani, M.; Giardino, C.; Alberotanza, L. The impact of the microphysical properties of aerosol on the atmospheric correction of hyperspectral data in coastal waters. *Atmos. Meas. Tech.* **2015**, *8*, 1593–1604.